

segregated, with  $\gamma$ -actin found predominantly in the stress fibers and  $\beta$ -actin predominantly at the leading edge (16–18). Because  $\beta$ -actin is arginylated to about 40% and  $\gamma$ -actin is not, the difference between  $\beta$ - and  $\gamma$ -actin-containing filaments in vivo should be quite substantial. Indeed, at the leading edge,  $\beta$ -actin-containing filaments are assembled from about 40% of arginylated subunits, which should prevent their side-to-side aggregation and induce the formation of a loose network, normally seen at the leading edge of locomoting cells. At the same time, the arrangement of arginylation-free  $\gamma$ -actin-containing filaments in the cell body favors the tightly packed stress fibers (Fig. 5D). Although other protein factors undoubtedly participate in this arrangement, the absence of arginylation in such cells should lead to bundling of  $\beta$ -actin at the leading edge, which would conceivably result in lamella collapse and the accumulation of  $\beta$ -actin aggregates in the cytoplasm, as seen in the *Ate1*<sup>-/-</sup> cells.

To further test these predictions, we have developed a mathematical model of actin assembly in vitro and in vivo in the presence and absence of arginylation (supporting online material). This model, in agreement with the experimental data and data from the literature, suggests that both  $\beta$ -actin arginylation and its targeting to the leading edge are essential to differentiate between actin isoform-specific networks in vivo and facilitate lamella formation in locomoting cells. The model also predicts that the effect of arginylation on actin assembly can be expected in a range of percentages of arginylated subunits as compared to nonarginylated ones, with effects that are substantial even when as little as 20% of the leading-edge actin is arginylated. Thus, our crude estimation of 40% arginylated  $\beta$ -actin does not need to be accurate to explain the observed effects in vivo and in vitro. In fact, the percentage of arginylated actin should vary in vivo, depending on the motile state of the cell.

Cell motility is critically important during cardiovascular development and angiogenesis. Our finding provides insights into the molecular events that lead to the impairment of these developmental events in *Ate1*<sup>-/-</sup> mice. Indeed, the defects in lamella formation observed in the *Ate1*<sup>-/-</sup> cells could result in reduced migration of the cells of cardiovascular lineages. Arginylation has been suggested to regulate many proteins; thus, other protein targets are likely to be responsible for additional arginylation defects on the molecular, cellular, and organismal levels.

#### References and Notes

- H. Kaji, G. D. Novelli, A. Kaji, *Biochim. Biophys. Acta* **76**, 474 (1963).
- H. Kaji, *Biochemistry* **7**, 3844 (1968).
- E. Balzi, M. Choder, W. N. Chen, A. Varshavsky, A. Goffeau, *J. Biol. Chem.* **265**, 7464 (1990).
- Y. T. Kwon *et al.*, *Science* **297**, 96 (2002).
- P. A. Rubenstein, D. J. Martin, *J. Biol. Chem.* **258**, 3961 (1983).
- P. A. Rubenstein, D. J. Martin, *J. Biol. Chem.* **258**, 11354 (1983).

- D. J. Martin, P. A. Rubenstein, *J. Biol. Chem.* **262**, 6350 (1987).
- D. R. Sheff, P. A. Rubenstein, *J. Biol. Chem.* **264**, 11491 (1989).
- S. Schmitz *et al.*, *J. Mol. Biol.* **295**, 1201 (2000).
- E. S. Hennessey, D. R. Drummond, J. C. Sparrow, *Eur. J. Biochem.* **197**, 345 (1991).
- P. A. Rubenstein, J. A. Spudich, *Proc. Natl. Acad. Sci. U.S.A.* **74**, 120 (1977).
- A. Bachmair, D. Finley, A. Varshavsky, *Science* **234**, 179 (1986).
- J. A. Cooper, T. D. Pollard, *Methods Enzymol.* **85**, 182 (1982).
- J. A. Cooper, S. B. Walker, T. D. Pollard, *J. Muscle Res. Cell Motil.* **4**, 253 (1983).
- K. C. Holmes, M. Tirion, D. Popp, M. Lorenz, W. Kabsch, R. A. Milligan, *Adv. Exp. Med. Biol.* **332**, 15 (1993).
- J. Condeelis, R. H. Singer, *Biol. Cell* **97**, 97 (2005).
- C. A. Otey, M. H. Kalnoski, J. L. Lessard, J. C. Bulinski, *J. Cell Biol.* **102**, 1726 (1986).
- D. Hofer, W. Ness, D. Drenckhahn, *J. Cell Sci.* **110**, 765 (1997).
- M. Lorenz, D. Popp, K. C. Holmes, *J. Mol. Biol.* **234**, 826 (1993).
- We are grateful to I. Sorokina from Midwest Bio Services for the original observation of the arginylated  $\beta$ -actin peptide and helpful suggestions throughout the project;

S. Zigmund, J. Pehrson, and V. Rodionov for helpful discussions; D. Dong for assistance in preparation of the arginylated actin database; B. He from W. Guo's lab for his help with setting up the actin polymerization assays and a gift of recombinant VCA; Y. Wolf for his help with the analysis of the actin crystal structure and preparation of Fig. 5; M. Crawford and the staff of the W. M. Keck Facility at Yale for help with the analysis of actin samples; and S. Zigmund for critical reading of the manuscript. This work was supported by grant PC040372 from the U.S. Department of Defense Congressionally Directed Medical Research Programs to A.K. and by NIH grant P41 RR11823-09 to J.R.Y.

#### Supporting Online Material

www.sciencemag.org/cgi/content/full/1129344/DC1  
Materials and Methods  
SOM Text  
Figs. S1 to S5  
Table S1  
References  
Videos S1 to S7

13 March 2006; accepted 24 May 2006

Published online 22 June 2006;

10.1126/science.1129344

Include this information when citing this paper.

## Massive-Star Supernovae as Major Dust Factories

Ben E. K. Sugerman,<sup>1\*</sup> Barbara Ercolano,<sup>2</sup> M. J. Barlow,<sup>2</sup> A. G. G. M. Tielens,<sup>3</sup> Geoffrey C. Clayton,<sup>4</sup> Albert A. Zijlstra,<sup>5</sup> Margaret Meixner,<sup>1</sup> Angela Speck,<sup>6</sup> Tim M. Gledhill,<sup>7</sup> Nino Panagia,<sup>1</sup> Martin Cohen,<sup>8</sup> Karl D. Gordon,<sup>9</sup> Martin Meyer,<sup>1</sup> Joanna Fabbri,<sup>2</sup> Janet. E. Bowey,<sup>2</sup> Douglas L. Welch,<sup>10</sup> Michael W. Regan,<sup>1</sup> Robert C. Kennicutt Jr.<sup>11</sup>

We present late-time optical and mid-infrared observations of the Type II supernova 2003gd in the galaxy NGC 628. Mid-infrared excesses consistent with cooling dust in the ejecta are observed 499 to 678 days after outburst and are accompanied by increasing optical extinction and growing asymmetries in the emission-line profiles. Radiative-transfer models show that up to 0.02 solar masses of dust has formed within the ejecta, beginning as early as 250 days after outburst. These observations show that dust formation in supernova ejecta can be efficient and that massive-star supernovae could have been major dust producers throughout the history of the universe.

Millimeter observations of high-redshift ( $z > 6$ ) quasars have revealed the presence of copious amounts of dust when the universe was as young as 700 million years (1). At the present day, dust in the interstellar medium of the Milky Way and other galaxies is generally thought to be injected mainly by the gentle winds of low-mass stars when they evolve onto the Asymptotic Giant Branch (2). However, stellar-evolution time scales of these low- to intermediate-mass stars are too long for them to have been a major contributor to the dust budget in the early universe (3). Instead, dust in the early universe must reflect the contribution from rapidly evolving (1 to 10 million years) massive stars, which return their nuclear ashes in explosive Type II supernova (SN) events. Theoretical studies have long suggested that dust can condense in the ejecta from core collapse (e.g., Type II) SNe (4), and calculations predict condensation of 0.08 to 1 solar mass ( $M_{\odot}$ ) of

dust within a few years, depending on metallicity and progenitor mass (5–7). There is also evidence for the origin of some dust in Type II

<sup>1</sup>Space Telescope Science Institute, 3700 San Martin Drive, Baltimore, MD 21218, USA. <sup>2</sup>Department of Physics and Astronomy, University College London, Gower Street, London WC1E 6BT, UK. <sup>3</sup>Kapteyn Astronomical Institute, Post Office Box 800, 9700 AV Groningen, Netherlands. <sup>4</sup>Department of Physics and Astronomy, Louisiana State University, Baton Rouge, LA 70803, USA. <sup>5</sup>School of Physics and Astronomy, University of Manchester, Post Office Box 88, Manchester M60 1QD, UK. <sup>6</sup>Department of Physics and Astronomy, University of Missouri, 316 Physics, Columbia, MO 65211, USA. <sup>7</sup>Department of Physics, Astronomy, and Maths, University of Hertfordshire, Hatfield AL10 9AB, UK. <sup>8</sup>Monterey Institute for Research in Astronomy, 200 Eighth Street, Marina, CA 93933, USA. <sup>9</sup>Steward Observatory, University of Arizona, 933 North Cherry Avenue, Tucson, AZ 85721, USA. <sup>10</sup>Department of Physics and Astronomy, McMaster University, Hamilton, Ontario L8S 4M1, Canada. <sup>11</sup>Institute of Astronomy, University of Cambridge, Madingley Road, Cambridge, CB3 0HA, UK.

\*To whom correspondence should be addressed. E-mail: sugerman@stsci.edu

SNe on the basis of the isotopic composition of stardust isolated in meteorites (8).

Direct observational evidence for efficient dust formation in SN ejecta is, however, lacking, largely because SN explosions are rare and far apart. Dust formation was detected in the ejecta of SNe 1987A and 1999em, but only some  $10^{-4} M_{\odot}$  were inferred for each (9–11), a factor up to  $10^3$  smaller than typical SNe would have had to produce in order to contribute efficiently to the early-universe dust budget (12). Similarly low dust masses have been measured in evolving SN remnants with the recently launched Spitzer Space Telescope (13); however, its mid-infrared (mid-IR) instruments are most sensitive to warm (50 to 500 K) material, whereas dust in these remnants has almost certainly cooled to  $<30$  K. Cold dust has been detected in remnants in the far-IR and sub-mm wavelengths; however, such observations risk strong contamination by cold, unrelated dust clouds along the line of sight (14). As such, the best way to demonstrate dust condensation in SN ejecta is to study them within a few years of their explosion, during the epoch of condensation when the ejecta are much hotter than interstellar dust. The high sensitivity of Spitzer's mid-IR detectors allows us to sample very young core-collapse SNe within  $\sim 20$  Mpc and opens up the whole nearby universe for such studies. Here we report on such a study of the Type II-P SN 2003gd in the galaxy NGC 628. A rare combination of contemporaneous optical and mid-IR observations of this well-studied SN with a known stellar progenitor mass of  $8^{+4}_{-2} M_{\odot}$  (15, 16) provides an excellent test case for the efficiency of dust formation in SN ejecta.

**Data in support of dust production.** As dust condenses in SN ejecta, it increases the internal optical depth of the expanding ejecta, producing three observable phenomena: (i) a mid-IR excess; (ii) asymmetric blue-shifted emission lines, because the dust obscures more emission from receding gas; and (iii) an increase in optical extinction. All of these were observed from 1 to 3 years after outburst in SN 1987A (9, 10). In this section, we present

or confirm all three phenomena from SN 2003gd.

NGC 628 was observed by the Spitzer Infrared Nearby Galaxies Survey (SINGS) Legacy program (17) with Spitzer Space Telescope's Infrared Array Camera (IRAC) at 3.6, 4.5, 5.8, and 8.0  $\mu\text{m}$  on 28 July 2004, or day 499 after outburst (18), and with the Multiband Imaging Spectrometer for Spitzer (MIPS) on 23 January 2005 (day 678) at 24  $\mu\text{m}$ ; the SN was also observed with IRAC as part of GO-3248 (P. I. W. P. Meikle) on 2005 Jan 15 (day 670). All data were acquired from the Spitzer archive, then spatially enhanced with the SINGS data pipelines to a final resolution of  $0.''75 \text{ pixel}^{-1}$ . A point source identified in all four IRAC bands from day 499 is consistent to within  $0.''17$  (0.2 IRAC pixels) with the position of the SN progenitor (Fig. 1), as measured by careful absolute and differential astrometry between the 3.6- $\mu\text{m}$  IRAC image and the archival Hubble Space Telescope (HST) Wide Field and Planetary Camera 2 (WFPC2) data in which the progenitor was identified (16).

Photometry of the Spitzer data was performed with point-spread-function fitting techniques (19). The resulting flux densities are  $20.8 \pm 2.6 \mu\text{Jy}$  at 3.6  $\mu\text{m}$ ,  $73.8 \pm 5.6 \mu\text{Jy}$  at 4.5

$\mu\text{m}$ ,  $64.9 \pm 7.3 \mu\text{Jy}$  at 5.8  $\mu\text{m}$ , and  $103 \pm 22 \mu\text{Jy}$  at 8.0  $\mu\text{m}$  on day 499, and  $106 \pm 16 \mu\text{Jy}$  at 24  $\mu\text{m}$  on day 678; the SN is nearly undetectable in IRAC on day 670, with  $3\sigma$  upper limits of 6.0, 10.6, 13.5, and 26.6  $\mu\text{Jy}$  at 3.6, 4.5, 5.8, and 8.0  $\mu\text{m}$ , respectively (Fig. 2). An excess at 4.5  $\mu\text{m}$  could be due to CO emitting at 4.6  $\mu\text{m}$  (10). Otherwise, the rising 5.8- to 24- $\mu\text{m}$  flux densities are not expected from the gaseous ejecta, which typically have temperatures of 3000 to 5000 K at these late times (10). It is unlikely that this emission is a thermal light echo, because the time variability of the IRAC fluxes is much faster than that expected for a typical circumstellar dust shell (20). Assuming that the mid-IR emission can be modeled with a single blackbody, the best fit to the 5.8- to 8.0- $\mu\text{m}$  data from day 499 has a temperature of 480 K, which for an adopted distance to the SN of 9.3 Mpc (18) yields an integrated luminosity of  $4.6 \times 10^5 L_{\odot}$  and an equivalent radius of  $6.8 \times 10^{15} \text{ cm}$ . The size, temperature, and variability implied by the spectral-energy distributions (SEDs) are thus consistent with lower temperature ( $T \sim 500$  K) dust that is cooling within the SN ejecta.

The first indication of such dust formation in SN 2003gd came in a comparison of broadband photometry and H $\alpha$  spectra of the SN

**Fig. 2.** Spectral-energy distribution of SN 2003gd, showing optical photometry on day 493 (squares) from (18) and extrapolated from day 632 (21) to day 678 (diamonds) based on the evolution of SN 1987A (24); IRAC data from day 499 (circles); upper limits to IRAC from day 670 (arrows); and the MIPS datum from day 678 (triangle). Error bars are computed with a Poisson-noise model that includes detector characteristics, and flat-field and profile uncertainties. Fluxes have been dereddened by  $E(B - V) = 0.14$  (18). The curves are MOCASSIN radiative-transfer model fits to the data at day 499 (solid lines) and 678 (dashed lines) based on smoothly distributed (black) and clumpy (gray) dust. See text and Table 2.

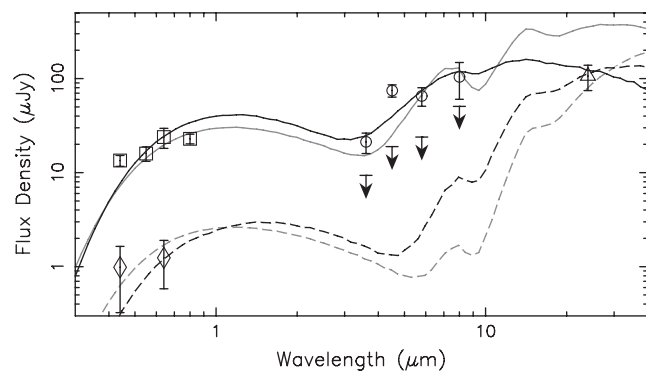
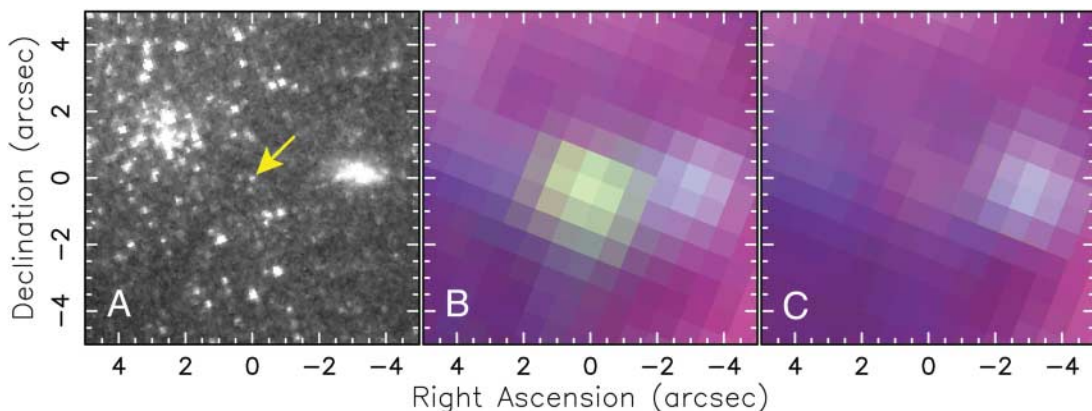


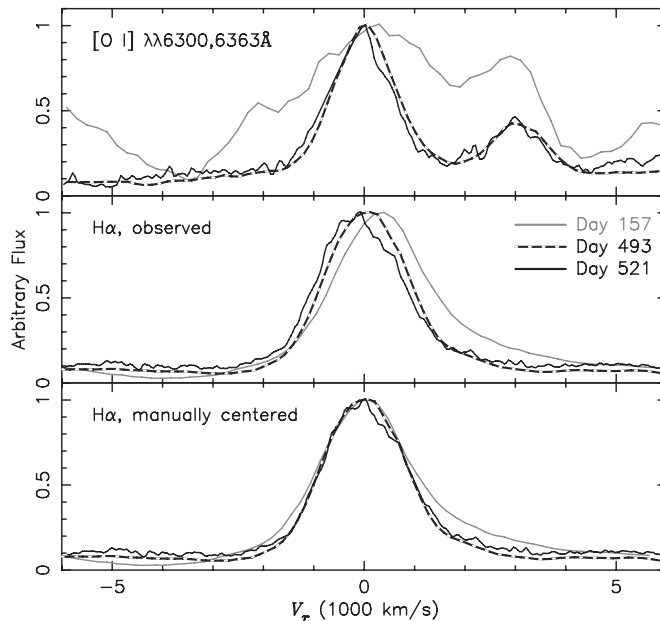
**Fig. 1.** Hubble and Spitzer Space Telescope images of a  $10''$  by  $10''$  field centered on the position of SN 2003gd. (A) HST WFPC2 image taken in the F606W filter in which the SN progenitor (arrow) was identified (15, 18), with a resolution of  $0.''045 \text{ pixel}^{-1}$ . (B and C) False-color SST IRAC images of the SN taken on (B) 28 July 2004 and (C) 15 January 2005, showing the 3.6- $\mu\text{m}$  (blue), 4.5- $\mu\text{m}$  (green), and 8.0- $\mu\text{m}$  (red). All IRAC images were processed by the SINGS collaboration to a final resolution of  $0.''75 \text{ pixel}^{-1}$ .



between days 124 and 493 (18), in which a small decline in the late-time luminosity was accompanied by a slight blueshift in the emission-line peaks. New spectroscopic observations of SN 2003gd were obtained in long-slit mode, covering  $\sim 4500$  to  $7000$  Å with a spectral resolution of  $\sim 7$  Å, by the Gemini Multi-Object Spectrograph (GMOS) on Gemini North on 19 August 2004 (day 521). Two spectra of SN 2003gd were obtained, which have been debiased, flattened, wavelength-calibrated, sky-subtracted, extracted, and then combined. The wavelength calibration is accurate to about 2 Å. The  $H\alpha$  and [O I] spectra from days 157 and 493 (18) are compared to the newer data in Fig. 3. Inspection of the lines confirms that the emission peak is indeed blueshifting, whereas the red high-velocity wing seen at the earliest epoch has diminished. Additionally, the most recent spectra show a clear asymmetry in the first few hundred  $\text{km s}^{-1}$  redward of each line peak. These blueshifted peaks and asymmetric profiles are consistent with a simple model in which dust with an increasing optical depth is located within an expanding sphere of uniform emission (11); in particular, the day 521 profiles suggest an optical extinction  $A_R < 5$ .

The  $B$ ,  $V$ , and  $R$  light curves of SN 2003gd through day 493 (18) have been combined with the  $B$ - and  $R$ -band photometry from day 632 (21) in Fig. 4. Over this 500-day period, the SN is evolving almost identically to SN 1987A, with the exception that SN 2003gd is slightly subluminal in  $V$  and  $R$  around day 493. The close match between the light curves of these two SNe implies an increase in optical extinction of SN 2003gd as well.

**Fig. 3.** Optical spectra of SN 2003gd showing [O I]  $\lambda\lambda 6300, 6363$  Å (top) and  $H\alpha$  (middle and bottom). Spectra have been corrected for the redshift  $z = 0.00219$  of galaxy NGC 628. The gray curves are taken from the data presented in (18), showing the profiles at days 157 (solid line) and 493 (broken line). The solid black curve is from the new data taken on day 521 with GMOS-N on Gemini North. The profiles are normalized to an arbitrary flux scale. A monotonic blueshift in the  $H\alpha$  line peak, first reported by (18), is confirmed. The most recent spectra in all three lines also show a clear profile asymmetry redward of each line peak. This evolution is expected from dust forming homogeneously within the ejecta, which preferentially extinguishes emission from the receding (i.e., redshifted) gas.



The observed dust extinction is measured by comparing the change in photometry over time to a standard intrinsic luminosity. The internal extinction in SN 1987A is believed to have increased by  $A_R = 0.8$  mag between days 525 and 700, as determined in broad-band photometry by comparing the light curve after day 525 to the best fit line through the data from days 450 to 525 (9). The slope of this line (Fig. 4) is extremely sensitive to the subset of the SN 1987A light curve used, and the resulting dust extinction can vary by  $>1$  mag depending on the days included in the least-squares fit. Thus, we deem this a poor measure of the intrinsic luminosity.

The broad-band evolution of Type II SNe past  $\sim 500$  days is poorly documented, because very few SNe have been observed beyond this epoch. At these late times, the light curve is dominated by the energy input of  $\gamma$ -rays from  $^{56}\text{Co}$  decay, which decreases with an  $e$ -folding time of  $\tau_{56} = 111.2$  days. The  $R$ -band photometry of the Type II SN 1990E (22) closely follows this evolution through 540 days (Fig. 4), suggesting that simple Co decay provides a good estimate of the unextinguished  $R$ -band light curve for at least that long. However, as the ejecta expand, their opacity to  $\gamma$ -rays is expected to decrease, which results in a modified light curve (23)

$$L_{56}(t) \propto e^{-t/\tau_{56}} [1 - e^{-\kappa_{56} \phi_0 (t_0/t)^2}] \quad (1)$$

where the term in brackets is the “effective opacity”;  $\kappa_{56} = 0.033 \text{ cm}^2 \text{ g}^{-1}$  is the average opacity to  $^{56}\text{Co}$ -decay  $\gamma$ -rays, and  $\phi_0 = 7 \times 10^4 \text{ g cm}^{-2}$  is the column depth at the fiducial time  $t_0 = 11.6$  days, chosen to match the bolometric

light curve of SN 1987A (23, 24). Note that Eq. 1 begins fading relative to simple  $^{56}\text{Co}$  decay around 500 days.

The Co-decay curves, both with and without the effective-opacity correction, are much more luminous than the aforementioned linear fit to SN 1987A at the time of dust formation (Fig. 4). The slopes of these Co-decay curves also closely resemble that of SN 1987A after day 775, when dust production is believed to have ended (10). Thus, Eq. 1 offers a more realistic standard luminosity for the unextinguished  $R$ -band light curve of SN 1987A. Comparison of  $L_{56}$  to the SN 1987A photometry yields extinctions of 1.5 mags around day 700 when effective opacity is included, and 2.5 mag when it is excluded. Because the evolution of SNe 1987A and 2003gd are so similar, Eq. 1 is also used to estimate the extinction of SN 2003gd at each epoch, as listed in Table 1.

#### Dust-mass analysis and interpretation.

The observations presented above overwhelmingly point toward dust forming within the ejecta of SN 2003gd, beginning sometime between 250 and 493 days after outburst. To estimate the mass of dust present, we use the three-dimensional Monte Carlo radiative-transfer code MOCASSIN (25). Briefly, the paths of photon absorption, scattering, and escape are followed from a specified source through a given composition, grain-size distribution, and geometry of dust. The particular choices of these are either constrained a priori or are varied until the model emission and extinction match the observed values.

Because our hypothesis is that dust condenses within the ejecta, the radiative-transfer model is constructed under the initial assumption that the dust and source luminosity are mixed within a spherical, expanding shell with inner radius  $r_{\text{in}}$ , outer radius  $Yr_{\text{in}}$ , and  $\rho \propto r^{-2}$  density profile, and with the illuminating radiation proportional to the dust density. Initial values for the shell size, source luminosity, and temperature are guided by the blackbody previously fit to the mid-IR data and by models

**Table 1.**  $R$ -band extinction of SN 2003gd. Equation 1 is used with and without the effective opacity term to estimate the average and maximal extinction, respectively. The observed values are listed first, and these were used along with the  $R$ -band light curve of SN 1987A to extrapolate the extinction of the SN at the epochs of SST observation.

Day	$A_R$ (mags)		
	Average	Maximal	Error
<i>Observed</i>			
493	0.52	0.73	0.09
632	1.36	1.78	0.12
<i>Extrapolated</i>			
499	0.53	0.74	0.14
678	1.51	2.13	0.20

of SN 1987A at similar epochs (10). There are numerous models for dust formation within SN ejecta [for a review, see (26)], most of which predict that grain sizes will remain small. We adopt a standard  $a^{-3.5}$  size distribution (27), with grain radii between 0.005 and 0.05  $\mu\text{m}$ , and the dust composition is taken to be 15% amorphous carbon and 85% silicates (7), with optical constants taken from (28, 29). Finally, because there are very few optical and mid-IR data to constrain a given model, the source luminosity is restricted to evolve according to Eq. 1, whereas its temperature remains constant (10).

Two dust distributions are considered. In the first, “smooth” model, the dust is uniformly distributed throughout the shell according to the adopted density profile. However, as early as a few hours after outburst, postshock ejecta become Rayleigh-Taylor unstable (30, 31), forming an inhomogeneous or “clumpy” distribution, which we model as a two-phase medium, in which spherical clumps with size  $r_c = \delta(Y r_{in})$ , volume filling factor  $f_c$ , and density contrast  $\alpha = \rho_c/\rho$  are embedded within an interclump medium of density  $\rho$ . This is analogous to the mega-grains approximation (32) with the addition of a radial density profile. Only macroscopic mixing has been found in the clumpy ejecta of SN remnant Cas A (33), which suggests that elemental ejecta layers remain heterogeneous. We therefore assume that the source luminosity is completely separated from the dust clumps. For a given geometry, a clumpy model will always require more mass than a smooth one to fit a given SED, because clumping lowers the overall optical depth for a given mass of dust (32). Rather than explore the extensive parameter space of clumpy models, we study the limiting case where all dust is in clumps, i.e.,  $\alpha \rightarrow \infty$ , which should provide upper mass limits, whereas the smooth models will provide lower mass limits. Finally, as suggested from hydrodynamic simulations (31), we fix  $\delta = 0.025$ .

Model results are summarized in Fig. 2 and Table 2. A good fit to the day 499 photometric and extinction data was achieved for the smooth model with  $Y = 7$ ,  $r_{in} = 5 \times 10^{15}$  cm,  $L = 6.6 \times 10^5 L_{\odot}$ , and  $T = 5000$  K, whereas fitting the day 678 data required changing  $r_{in}$  to  $6.8 \times 10^{15}$  cm and  $L$  to  $9.2 \times 10^4 L_{\odot}$ . Clumpy models used these same parameters, with  $f_c = 0.02$  on day 499, and  $f_c = 0.05$  on day 678. A

complete exploration of the model parameter space is beyond the scope of this work and will be presented elsewhere. In general, small changes to the model parameters have only modest effects. For example, including maximum grain sizes up to 0.25  $\mu\text{m}$  (typical of dust in the interstellar medium) decreases the dust mass by less than 10%. A 10% change in  $\delta$  or  $f_c$  results in a 1 to 5% change in mass for our adopted parameter ranges. Thus, the smooth and clumpy model results shown in Table 2 offer reasonably robust lower and upper mass limits, respectively.

These clumpy-model masses, up to  $2 \times 10^{-3} M_{\odot}$  on day 499 and  $2 \times 10^{-2} M_{\odot}$  on day 678, are much higher than most analytic estimates of the dust mass for SN 2003gd. For example, when the same grain properties as those above are used,  $5 \times 10^{-4}$  and  $2 \times 10^{-3} M_{\odot}$  of dust are required to produce the mid-IR emission at days 499 and 678, if all grains are visible and isothermal (34). When we use the mega-grains approximation for dust uniformly mixed with diffuse emission within a spherical shell (32), the  $R$ -band extinction yields masses of only  $10^{-5}$  and  $4 \times 10^{-4} M_{\odot}$  of smooth dust for days 499 and 678. In contrast, up to  $5 \times 10^{-3} M_{\odot}$  of clumpy dust is deduced from the mega-grains model for day 499, which agrees well with our radiative-transfer model. However, once clumps become optically thick, only geometry ( $\delta$ ,  $f_c$ ) determines their extinction, and thus an arbitrarily large mass of clumpy dust reproduces the extinction from day 678. This behavior of the mega-grains model makes it of limited use in determining dust masses when the observed optical depth reaches unity. We conclude that the most-often used analytic approximations can provide unreliable estimates of dust masses.

Observations similar to those presented here have demonstrated the condensation of dust in the ejecta of SN 1987A and 1999em, but the inferred masses for these SNe were only modest, on the order of  $10^{-4} M_{\odot}$  (10, 11). Asymmetric  $H\alpha$  line profiles have been de-

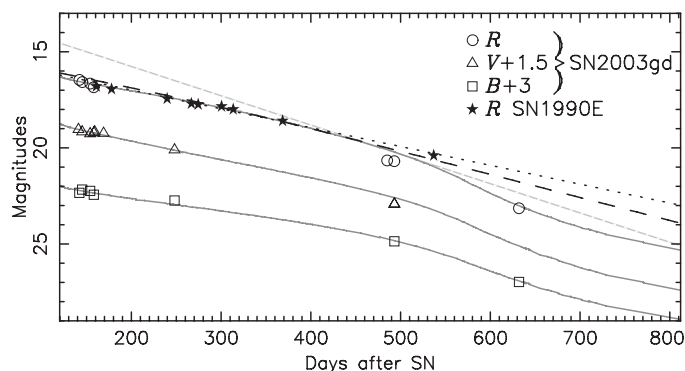
tected for Type II SNe 1970G, 1979C, and 1980K (35); however, this phenomenon on its own is also consistent with an expanding ionization front shell of emission catching up with and passing through a preexisting dust shell and does not prove the presence of newly forming dust. For SN 1998S, asymmetric line profiles and near-IR ( $\lambda < 4.7 \mu\text{m}$ ) excess emission also point toward dust condensation in the ejecta (36). In all these cases, the absence of contemporaneous mid-IR observations precluded a quantitative estimate of the condensation efficiency. In light of our quantitative clumpy-dust analysis, the amounts of dust believed to have formed in the ejecta of SN 1987A and 1999em—which were based upon analytical estimates—are being carefully revisited.

For a progenitor mass for SN 2003gd between 10 and 12  $M_{\odot}$  (18), roughly 0.16 to 0.42  $M_{\odot}$  of refractory elements are expected to form if the progenitor had solar metallicity (37). Assuming dust formation has finished by day 678, our derived dust mass of  $2 \times 10^{-2} M_{\odot}$  for this progenitor translates into a condensation efficiency, defined here as (mass of refractory elements condensed into dust)/(mass of refractory elements in ejecta), of  $\leq 0.12$  for clumpy dust. Having found that analytic analyses of optical and IR observations tend to underestimate the dust mass by an order of magnitude or more, we deem it likely that dust formation in core-collapse SNe is much more efficient than previously believed. In particular, the efficiency implied by SN 2003gd is close to the value of 0.2 needed for SNe to account for the dust content of high-redshift galaxies (12). As noted earlier, too few SNe have been followed sufficiently in time and wavelength to establish the frequency with which SNe form dust. We are currently addressing this question through continued, long-term monitoring of a much larger sample of young, Type II SNe. If dust formation is found to be common in core-collapse SNe, then because most dust is expected to survive later passage through high-velocity SN shocks (38), we can conclude that

**Table 2.** Dust masses and  $R$ -band extinction calculated by the radiative-transfer code MOCASSIN.

Day	Model	$A_R$	$M_{\text{dust}} (M_{\odot})$
499	Smooth	0.40	$2.0 \times 10^{-4}$
499	Clumpy	0.65	$1.7 \times 10^{-3}$
678	Smooth	1.48	$2.7 \times 10^{-3}$
678	Clumpy	1.22	$2.0 \times 10^{-2}$

**Fig. 4.** Light curves of SN 2003gd, showing the increase of extinction with time.  $B$ ,  $V$ , and  $R$  light curves of SN 2003gd compiled from (18) through day 493 after outburst, and (21) for day 632, are plotted and offset as marked. Error bars are all smaller than the point markers. For comparison, the corresponding light curves of SN 1987A (24) are also shown as thick gray lines, and the  $R$ -band light curve of SN 1990E is shown as filled stars. Also plotted in black are the light curves expected from Eq. 1 with (dashed) and without (dotted) the effective opacity term, as well as the linear fit to SN 1987A from days 450 to 525 (dashed gray) used by (9).



core-collapse SNe played an important role in the production of dust in the early universe.

#### References and Notes

1. F. Bertoldi *et al.*, *Astron. Astrophys.* **406**, L55 (2003).
2. A. G. G. M. Tielens, *Astrophys. J.* **499**, 267 (1998).
3. E. Dwek, *Astrophys. J.* **501**, 643 (1998).
4. F. Cernuschi, F. R. Marsicano, I. Kimel, *Ann. Astrophys.* **28**, 860 (1965).
5. E. Dwek, *Astrophys. J.* **329**, 814 (1988).
6. T. Kozasa, H. Hasegawa, K. Nomoto, *Astrophys. J.* **344**, 325 (1989).
7. P. Todini, A. Ferrara, *Mon. Not. R. Astron. Soc.* **325**, 726 (2001).
8. D. D. Clayton, S. Amari, E. Zinner, *Astrophys. Space Sci.* **251**, 355 (1997).
9. L. B. Lucy, I. J. Danziger, C. Guiffes, P. Bouchet, in *Supernovae. The Tenth Santa Cruz Workshop in Astronomy and Astrophysics*, S. E. Woosley, Ed. (Springer-Verlag, New York, 1991), p. 82.
10. D. H. Wooden *et al.*, *Astrophys. J. Suppl. Ser.* **88**, 477 (1993).
11. A. Elmhamdi *et al.*, *Mon. Not. R. Astron. Soc.* **338**, 939 (2003).
12. H. L. Morgan, M. G. Edmunds, *Mon. Not. R. Astron. Soc.* **343**, 427 (2003).
13. D. C. Hines *et al.*, *Astrophys. J. Suppl. Ser.* **154**, 290 (2004).
14. O. Krause *et al.*, *Nature* **432**, 596 (2004).
15. S. D. Van Dyk, W. Li, A. V. Filippenko, *Publ. Astron. Soc. Pac.* **115**, 1289 (2003).
16. S. J. Smartt *et al.*, *Science* **303**, 499 (2004).
17. R. C. Kennicutt Jr. *et al.*, *Publ. Astron. Soc. Pac.* **115**, 928 (2003).
18. M. A. Hendry *et al.*, *Mon. Not. R. Astron. Soc.* **359**, 906 (2005).
19. P. B. Stetson, *Publ. Astron. Soc. Pac.* **99**, 191 (1987).
20. E. Dwek, *Astrophys. J.* **274**, 75 (1983).
21. B. E. K. Sugerman, *Astrophys. J.* **632**, L17 (2005).
22. S. Benetti *et al.*, *Astron. Astrophys.* **285**, 147 (1994).
23. S. E. Woosley, D. Hartmann, P. A. Pinto, *Astrophys. J.* **346**, 395 (1989).
24. N. B. Suntzeff, P. Bouchet, *Astron. J.* **99**, 650 (1990).
25. B. Ercolano, M. J. Barlow, P. J. Storey, *Mon. Not. R. Astron. Soc.* **362**, 1038 (2005).
26. D. D. Clayton, L. R. Nittler, *Annu. Rev. Astron. Astrophys.* **42**, 39 (2004).
27. J. S. Mathis, W. Ruml, K. H. Nordsieck, *Astrophys. J.* **217**, 425 (1977).
28. B. T. Draine, H. M. Lee, *Astrophys. J.* **285**, 89 (1984).
29. M. S. Hanner, *NASA Conf. Pub.* **3004**, 22 (1988).
30. R. A. Chevalier, R. I. Klein, *Astrophys. J.* **219**, 994 (1978).
31. M. Herant, S. E. Woosley, *Astrophys. J.* **425**, 814 (1994).
32. F. Városi, E. Dwek, *Astrophys. J.* **523**, 265 (1999).
33. T. Douvion, P. O. Lagage, C. J. Cesarsky, *Astron. Astrophys.* **352**, L111 (1999).
34. S. D. Doty, C. M. Leung, *Astrophys. J.* **424**, 729 (1994).
35. R. A. Fesen *et al.*, *Astron. J.* **117**, 725 (1999).
36. M. Pozzo *et al.*, *Mon. Not. R. Astron. Soc.* **352**, 457 (2004).
37. S. E. Woosley, T. A. Weaver, *Astrophys. J. Suppl. Ser.* **101**, 181 (1995).
38. T. Nozawa, T. Kozasa, A. Habe, <http://arxiv.org/abs/astro-ph/0605193>.
39. We gratefully acknowledge M. Hendry for providing optical spectra of SN 2003gd, and E. Dwek and P. Ghavamian for useful discussions. This work is based in part on archival data obtained with the Spitzer Space Telescope, which is operated by the Jet Propulsion Laboratory, California Institute of Technology, under a contract with NASA; with the NASA/European Space Agency Hubble Space Telescope, obtained from the Data Archive at the Space Telescope Science Institute, which is operated by the Association of Universities for Research in Astronomy, Inc. (AURA), under NASA contract NAS 5-26555; and on observations obtained during the program GN-2004B-C-3 at the Gemini Observatory, which is operated by AURA under a cooperative agreement with the NSF on behalf of the Gemini partnership. Support for B.E.K.S. for this work was provided by Spitzer Space Telescope award GO-20320 issued by the Jet Propulsion Laboratory/California Institute of Technology (JPL/Caltech). D.L.W. acknowledges support from the Natural Sciences and Engineering Research Council of Canada. M.C.'s participation was supported by JPL contract 1269553 with the Monterey Institute for Research in Astronomy.

30 March 2006; accepted 30 May 2006  
Published online 8 June 2006;  
10.1126/science.1128131  
Include this information when citing this paper.

## REPORTS

# Electric Fields at the Active Site of an Enzyme: Direct Comparison of Experiment with Theory

Ian T. Suydam, Christopher D. Snow, Vijay S. Pande, Steven G. Boxer\*

The electric fields produced in folded proteins influence nearly every aspect of protein function. We present a vibrational spectroscopy technique that measures changes in electric field at a specific site of a protein as shifts in frequency (Stark shifts) of a calibrated nitrile vibration. A nitrile-containing inhibitor is used to deliver a unique probe vibration to the active site of human aldose reductase, and the response of the nitrile stretch frequency is measured for a series of mutations in the enzyme active site. These shifts yield quantitative information on electric fields that can be directly compared with electrostatics calculations. We show that extensive molecular dynamics simulations and ensemble averaging are required to reproduce the observed changes in field.

The organization of charged and polar groups in the folded state of proteins produces large electric fields that influence nearly every aspect of protein function. Electrostatics calculations suggest that these fields vary markedly from site to site in magnitude and direction (1–3). The consequence of such variations can be appreciated by considering a dipolar transition state that separates a unit charge over a distance of 1 Å. If this dipole were parallel to a field of 10 MV/cm, not

atypical of fields that are estimated to be present in proteins, the energy of the transition state would be lowered by 9.6 kJ/mol; thus, the magnitude and direction of the field could have a substantial effect on the rate of reaction. Simulations on a large number of enzymes support this hypothesis and have shown that preorganized electric fields in active sites contribute substantially to transition-state stabilization (4).

Colorful maps of electrostatic potentials are routinely included in papers describing or analyzing protein structures and are often used to speculate on the electrostatic contributions to a variety of protein functions. However, there are relatively few experiments that can be used to test these calculations directly. Common

benchmarks related to changes in free energies, such as  $pK_a$  shifts (where  $K_a$  is the acid dissociation constant), redox potential shifts, or binding constants, depend on a convolution of factors including electrostatic interactions, making direct comparisons to calculated potentials difficult. Similarly, electrostatic interactions can contribute substantially to the effect of mutations on the rates of enzyme-catalyzed reactions, but it is difficult to isolate their contribution.

In contrast, spectroscopic observables that relate directly to electric fields provide a straightforward connection to calculated potentials (5, 6). The vibrational Stark effect, which describes the effect of an electric field on a molecular vibration, provides a particularly straightforward approach. The vibrational Stark tuning rate gives the sensitivity of a probe vibration to an electric field and can be calibrated by measuring the vibrational Stark spectrum in a known external electric field (7, 8). Once calibrated, a probe vibration acts as a local reporter of its electrostatic environment; its frequency shifts in response to changes in nearby amino acids or protonation states, offering a direct measurement of the electric field change at specific sites. For many vibrations, the effect of an electric field on the stretching frequency is dominated by the projection of  $D\vec{m}_{\text{probe}}$ , the change in dipole moment between the ground and excited states of the probe transition, along the electric field vector (8–12)

$$hcD\vec{m}_{\text{obs}} = -D\vec{m}_{\text{probe}} \cdot D\vec{F}_{\text{protein}} \quad (1)$$

Department of Chemistry, Stanford University, Stanford, CA 94305–5080, USA.

\*To whom correspondence should be addressed. E-mail: sboxer@stanford.edu